



ELSEVIER

Contents lists available at ScienceDirect

## Journal of Magnetism and Magnetic Materials

journal homepage: [www.elsevier.com/locate/jmmm](http://www.elsevier.com/locate/jmmm)

# Computational analysis of magnetic field induced deposition of magnetic particles in lung alveolus in comparison to deposition produced with viscous drag and gravitational force

Andrej Krafcik<sup>a,\*</sup>, Peter Babinec<sup>b</sup>, Ivan Frollo<sup>a</sup>

<sup>a</sup> Institute of Measurement Science, Slovak Academy of Sciences, Dúbravská cesta 9, 841 04 Bratislava, Slovakia

<sup>b</sup> Faculty of Mathematics, Physics and Informatics, Comenius University, Mlynska dolina F1, 842 48 Bratislava, Slovakia



## ARTICLE INFO

## Article history:

Received 19 June 2014

Received in revised form

3 October 2014

Accepted 4 October 2014

Available online 13 October 2014

## Keywords:

Aerosol droplet with SPION

Cylindrical Halbach array

FEM

Lung alveoli

Magnetically induced particles deposition

Simulation

Targeting

## ABSTRACT

Magnetic targeting of drugs attached to magnetic nanoparticles with diameter  $\approx 100$  nm after their intravenous administration is an interesting method of drug delivery widely investigated both theoretically as well as experimentally. Our aim in this study is theoretical analysis of a magnetic aerosol targeting to the lung. Due to lung anatomy magnetic particles up to  $5 \mu\text{m}$  can be safely used, therefore the magnetic force would be stronger, moreover drag force exerted on the particle is according to Stokes law linearly dependent on the viscosity, would be weaker, because the viscosity of the air in the lung is approximately 200 fold smaller than viscosity of the blood. Lung therefore represents unique opportunity for magnetic drug targeting, as we have shown in this study by the analysis of magnetic particle dynamics in a rhythmically expanding and contracting distal and proximal alveolus subjected to high-gradient magnetic field generated by quadrupolar permanent Halbach magnet array.

© 2014 Elsevier B.V. All rights reserved.

## 1. Introduction

Lung cancer is the most common cause of cancer death worldwide with more than 1.3 million people dying of the disease annually, which represents 23% of total cancer deaths. The respiratory system has a large surface area ( $>100\text{m}^2$ ), thin alveolar epithelium, rapid absorption, lack of first-pass metabolism, high bioavailability, and the capacity to absorb large quantities of drugs, making aerosolized drug or gene delivery an optimal route of administration [1]. Interest in utilizing gene therapy to treat pulmonary diseases such as acute respiratory distress syndrome, cancer, asthma, emphysema, and cystic fibrosis has increased in recent years [2–4]. Inhalation of aerosols represents the most frequently used drug delivery method for the treatment of lung diseases. To further improve drug efficacy in the lungs, it may be advantageous to control aerosol deposition and target aerosols using magnetic gradient fields [5–13] to direct magnetizable aerosol droplets containing superparamagnetic iron oxide nanoparticles specifically to desired regions of the lungs in mice to decrease harmful side effects and increase treatment efficacy. In a recent study [14] quadrupolar magnetic field has been successfully

used for these purposes. Magnetic quadrupole is a kind of Halbach cylindrical array, which is a magnetized cylinder composed of ferromagnetic material producing an intense magnetic field confined entirely within the cylinder with zero field outside [15]. Moreover quadrupolar magnets with gradients higher than  $100 \text{ T/m}$  are widely used for beam focusing in linear accelerators and are even commercially available [16], therefore it would not be a problem to use them for *in vivo* therapeutic purposes. For the prediction of particle transport and deposition, and for the development of effective drug delivery strategies for the lung, it is the most important to understand flow phenomena on the alveolar level [17–19]. Our aim in this study is to analyze theoretically behavior of aerosolized magnetic nanoparticles in alveoli under the influence of quadrupolar magnetic field and compare the effect of magnetic field with that of earth gravitational field and aerodynamic viscous drag force.

## 2. Physical model

### 2.1. Particle motion—forces affecting particle

The differential equation governing the motion of a spherical particle with mass  $m_p$  and a nonzero magnetic moment  $\mu_p$  subjected to gravity field with gravitational acceleration vector  $\mathbf{g}$

\* Corresponding author. Tel.: +421 2 591045 46.

E-mail addresses: [andrej.krafcik@savba.sk](mailto:andrej.krafcik@savba.sk) (A. Krafcik), [babinec@fmph.uniba.sk](mailto:babinec@fmph.uniba.sk) (P. Babinec), [ivan.frollo@savba.sk](mailto:ivan.frollo@savba.sk) (I. Frollo).

and external magnetic field with magnetic flux density  $\mathbf{B}$  is

$$m_p \frac{d\mathbf{v}_p}{dt} = \mathbf{F}_D + m_p \mathbf{g} + (\boldsymbol{\mu}_p \cdot \nabla) \mathbf{B} + \mathbf{F}_{Br}, \quad (1)$$

where  $\mathbf{v}_p$  is the particle velocity, and  $\mathbf{F}_D$  and  $\mathbf{F}_{Br}$  are the Stokes viscous drag and stochastic Brownian forces exerted on the particle, respectively. Henceforth, we focus on the combined deterministic effects of convection, sedimentation and targeting, and neglect the stochastic Brownian forces (see for instance [20]).

2.1.1. Drag forces

The drag force exerted on a spherical particle suspended in Stokesian flow field (Reynolds number is low, i.e.  $Re \ll 1$ )  $\mathbf{v}_f$  is given as

$$\mathbf{F}_D = 3\pi\eta_f D_p (\mathbf{v}_f - \mathbf{v}_p)_{CV} / C, \quad (2)$$

where  $\eta_f$  is the air dynamic viscosity (18.6  $\mu\text{Pa s}$  at 30  $^\circ\text{C}$ ), the suffix CV stands for evaluation of the airflow at the particle's center of volume.  $C$  is the slip correction factor for very small particles (less than 1.0  $\mu\text{m}$  in diameter), while for bigger particles it approaches 1.0 (e.g., for particles 0.5 and 1.0  $\mu\text{m}$  in diameter, it is 1.324 and 1.164, respectively).

*Alveolar Flow Model:* We have adapted the model proposed in [18] for our purposes. It views a single-alveolus configuration as a hemispherical cavity attached at rim to a flat plane (Fig. 1). The flow passing through the alveolar duct near the alveolus is approximated by a simple oscillatory shear flow over the flat plane, far upstream or downstream from the hemispherical cavity. The plane and the attached cavity perform an oscillatory, self-similar expansion and contraction movement. Assuming that the flow field is governed by the creeping flow equations, superposition of the following two flow fields is allowed: (1) *expansion flow*—the flow induced by the self-similar expansion and contraction of the alveolus with zero downstream flow inside the adjacent airway, and (2) *shear flow*—the flow induced by shear flow over a hemispherical rigid cavity with vanishing velocity at the boundaries. Moreover, due to the quasi-steadiness of Stokes flows, the time variable can be viewed as a parameter that enters the problem via time dependent boundary conditions. Thus, two generic problems are addressed: the flow field  $\mathbf{v}^H$  induced by a unit surface radial velocity for a unit radius hemisphere [17], and the flow field  $\mathbf{v}^P$  induced by a unit shear flow over a unit hemispherical cavity [21]. The solution representations for  $\mathbf{v}^H$  and  $\mathbf{v}^P$  are provided below in this section.

The flow  $\mathbf{v}_f$  inside the alveolus, which combines the effects of expanding and contracting alveolus and shear-induced flow generated by the airflow in the adjacent duct, is

$$\mathbf{v}_f = \dot{R}(t)\mathbf{v}^H + R(t)G(t)\mathbf{v}^P, \quad (3)$$

where  $\mathbf{v}^H$  and  $\mathbf{v}^P$  are multiplied by their respective time protocols for alveolus expansion and contraction,  $\dot{R}(t)$ , and for the oscillating shear flow in the adjacent airway,  $R(t)G(t)$ , where  $G(t)$  is the instantaneous shear rate at the airway wall. It is often treated (albeit not exact)  $R(t) = R_0[1 + \beta \cos(\omega t)]$ , and consequently,  $\dot{R}(t) = -R_0\beta\omega \sin(\omega t)$ , where  $\omega$  is the breathing frequency,  $R_0$  is the mean radius of the alveolus, and  $R_0\beta$  is the expansion amplitude. The time protocol is assumed to possess an identical  $\omega$  and a small phase difference  $\delta$  ( $\approx 10^\circ$ ; see [22]). The value of  $G_0$  depends on the breathing volumetric flow and the alveolus location down the acinar tree. The ratio of the shear and expansion flow amplitudes is given by  $\gamma = G_0/\beta\omega$ . From acinar morphology data [23], the value of  $\gamma$  at the first few generations from the entrance of the acinus (e.g., 16–19th) is  $>1000$  and remains  $>100$  for the most of the acinar generations, suggesting that the ductal shear flow plays an important role in determining alveolar flow [18].

*Expansion Flow Velocity Vector Field  $\mathbf{v}^H$*  [17]: Alveolus is represented as a spherical cap of radius  $R$  and is attached at its rim to a circular opening of radius  $a$  in an infinite plane. During the rhythmic process of expansion and contraction the half-conical angle  $\eta_0$  (Fig. 1) is held constant for all values of time—configuration in self-similar mode (the rate  $\dot{R}$  at which the radius changes also governs the rate at which the plane expands laterally). The flow dynamics of such rhythmically expanding and contracting alveolus are governed by the quasi-static Stokes equation for incompressible fluids with boundary conditions for a flow adhering to the moving boundaries of the cap and the plane (for details see [17]). This problem configuration is better suited in polar toroidal coordinates  $(\xi, \eta, \phi)$  defined according to [24] as

$$z = a \frac{\sin \eta}{\cosh \xi - \cos \eta}, \quad \rho = a \frac{\sinh \xi}{\cosh \xi - \cos \eta} \quad (4)$$

(for  $0 \leq \eta \leq 2\pi, 0 \leq \xi \leq \infty$ ), where spherical cap and axis of symmetry is given by  $\eta = \eta_0 < \pi$  and  $\xi = 0$ , respectively (see Fig. 1), and the plane with central circular hole corresponds to  $\eta = 2\pi$ . The  $(\rho, z, \phi)$  denotes the coordinates in polar cylindrical coordinate system.

By solving this problem (details in [17]) for unit hemisphere as alveolus model ( $\eta_0 = \pi/2, a=1$ ) we get the non-dimensional components of  $\mathbf{v}^H$  in polar toroidal coordinate system as

$$\begin{aligned} v_\xi^H = & - \frac{\sinh \xi (\cosh \xi \cos \eta - 2 \sin^2 \eta - 1)}{(\cosh \xi - \cos \eta)^2} - \frac{3}{2} \sin \eta \\ & \tanh(\xi/2) \left( \frac{1 - \cos \eta}{\cosh \xi - \cos \eta} \right)^{1/2} + \frac{3}{2} \frac{\sin \eta \sinh \xi}{(\cosh \xi - \cos \eta)^{1/2}} \\ & \cdot \int_0^\infty F_h(\alpha, \eta) P'_{-1/2+i\alpha}(\cosh \xi) \\ & d\alpha - \sinh \xi (\cosh \xi - \cos \eta)^{1/2} \\ & \cdot \int_0^\infty \frac{\partial F_h(\alpha, \eta)}{\partial \eta} P'_{-1/2+i\alpha}(\cosh \xi) d\alpha, \end{aligned} \quad (5a)$$

$$\begin{aligned} v_\eta^H = & \frac{\sin \eta (-\cosh^2 \xi - 2 \cos \eta \cosh \xi + 3)}{(\cosh \xi - \cos \eta)^2} \\ & - \frac{3}{2} \frac{(1 - \cos \eta)^{3/2}}{(\cosh \xi - \cos \eta)^{1/2}} \\ & + \frac{(\cosh^2 \xi - 4 \cosh \xi \cos \eta + 3)}{2(\cosh \xi - \cos \eta)^{1/2}} \\ & \cdot \int_0^\infty F_h(\alpha, \eta) P''_{-1/2+i\alpha}(\cosh \xi) d\alpha \\ & + \sinh^2 \xi (\cosh \xi - \cos \eta)^{1/2} \\ & \cdot \int_0^\infty F_h(\alpha, \eta) P''_{-1/2+i\alpha}(\cosh \xi) d\alpha, \end{aligned} \quad (5b)$$

where functions  $P'_{-1/2+i\alpha}(s)$  and  $P''_{-1/2+i\alpha}(s)$  are the 1st and 2nd derivative, respectively, with respect to  $s$  of the Legendre function of complex degree,  $P_{-1/2+i\alpha}(s)$  [25], and  $F_h(\alpha, \eta)$  is the representation function for hemispherical alveolus defined as

$$\begin{aligned} F_h(\alpha, \eta) = & \cos \eta \left[ A(\alpha) \frac{\cosh[(2\pi - \eta)\alpha]}{\cosh(\frac{3}{2}\pi\alpha)} + B(\alpha) \frac{\sinh[(2\pi - \eta)\alpha]}{\sinh(\frac{3}{2}\pi\alpha)} \right] \\ & - \sin \eta \left[ C(\alpha) \frac{\cosh[(2\pi - \eta)\alpha]}{\cosh(\frac{3}{2}\pi\alpha)} + D(\alpha) \frac{\sinh[(2\pi - \eta)\alpha]}{\sinh(\frac{3}{2}\pi\alpha)} \right], \end{aligned} \quad (6)$$

with coefficients  $A, B, C,$  and  $D$  of expression

$$A(\alpha) = 0, \tag{7a}$$

$$B(\alpha) = -\frac{G + E\alpha \coth(\frac{3}{2}\pi\alpha)}{1 - \alpha^2 / \sinh^2(\frac{3}{2}\pi\alpha)}, \tag{7b}$$

$$C(\alpha) = -\alpha B \coth(\frac{3}{2}\pi\alpha), \tag{7c}$$

$$D(\alpha) = -\frac{E(1 + \alpha^2) + G\alpha \coth(\frac{3}{2}\pi\alpha)}{1 - \alpha^2 / \sinh^2(\frac{3}{2}\pi\alpha)}. \tag{7d}$$

Coefficients  $E$  and  $G$  in (7) are defined for hemispherical alveolus as

$$E(\alpha) = \frac{4}{\sqrt{2}} \frac{\alpha^2 \cosh(\frac{1}{2}\pi\alpha)}{\alpha^2 + \frac{1}{4} \cosh(\pi\alpha)}, \tag{8a}$$

$$G(\alpha) = -\frac{4}{\sqrt{2}} \alpha \frac{\sinh(\frac{1}{2}\pi\alpha)}{\cosh(\pi\alpha)} + \frac{3}{\sqrt{2}} \frac{\alpha \sinh(\frac{1}{2}\pi\alpha)}{\alpha^2 + \frac{1}{4} \cosh(\pi\alpha)}. \tag{8b}$$

The solution (5b) for  $\mathbf{v}^H$  that was derived analytically [17] is axisymmetric and has only two independent velocity components in polar toroidal coordinate system  $v_\xi^H$  and  $v_\eta^H$  which after transformation to polar cylindrical coordinate system (see [24]) give velocity components  $v_\rho^H$  and  $v_z^H$  in the radial and axial directions,  $\rho$  and  $z,$  respectively, that can be evaluated in each  $(\rho, z)$  point. Thus, in a Cartesian coordinate system,  $\mathbf{v}^H$  possesses the form

$$\mathbf{v}^H = \begin{bmatrix} v_\rho^H(\rho, z) \cos \phi \\ v_\rho^H(\rho, z) \sin \phi \\ v_z^H(\rho, z) \end{bmatrix}, \tag{9}$$

where the  $\phi$  is the polar angle.

*Shear Flow Velocity Vector Field  $\mathbf{v}^P$*  [21]: Steady share flow over a plane wall that possesses a rigid cavity in the form of hemispherical cap was studied by Pozrikidis in [21] employing a numerical boundary integral method [26]. The numerical procedure was greatly simplified because the analytic dependence of velocity on the polar angle  $\phi$  had been known *a priori*. Consequently, the velocity field depends on the three independent unknown functions of the coordinates  $(\rho, z)$  to be determined numerically (see \code{06\_stokes|flow\_3x} directory in [27]). The solution possesses the

general following form in Cartesian coordinates

$$\mathbf{v}^P = \begin{bmatrix} v_1^P(\rho, z) \cos^2 \phi + v_2^P(\rho, z) \\ v_1^P(\rho, z) \cos \phi \sin \phi \\ v_3^P(\rho, z) \cos \phi \end{bmatrix}, \tag{10}$$

where the undisturbed shear flow far from the cavity points in the  $x$  direction. The 3D solution for  $\mathbf{v}^P$  obtained by Pozrikidis (that is defined for unity depression radius and unit shear rate) can be utilized to solve the quasi-steady problem for alternating shear rates embedded in time protocols.

*Drag Force Given by Velocity Vector Fields:* The quasi-steady solution (3) for the velocity vector field  $\mathbf{v}_r(x, y, z)$  was obtained for a unit hemisphere, whereas the alveolar radius in our case is not a unit and varies with time. Thus the instantaneous coordinates of the particle center  $\mathbf{r}_p = (x_p, y_p, z_p)$  must be normalized with the instantaneous radius  $R(t)$  and only than introduced into (3) to yield the proper velocity field that the particle encounters. Namely, the approximate drag force exerted on the particle in its center of volume is given by

$$\mathbf{F}_D = \frac{3\pi\eta_f D_p}{C} \left\{ \mathbf{v}_f \left[ \frac{x_p}{R(t)}, \frac{y_p}{R(t)}, \frac{z_p}{R(t)} \right] - \mathbf{v}_p \right\}, \tag{11}$$

or, after introducing (3) and time protocols mentioned previously into (11), yields

$$\mathbf{F}_D = -\frac{3\pi\eta_f D_p}{C} \left\{ R_0 \beta \omega \left[ \sin(\omega t) \mathbf{v}^H \left( \frac{\mathbf{r}_p}{R(t)} \right) + \gamma \sin(\omega t + \delta) \mathbf{v}^P \left( \frac{\mathbf{r}_p}{R(t)} \right) \right] + \frac{d\mathbf{r}_p}{dt} \right\}. \tag{12}$$

### 2.1.2. Magnetic force

Particle with the nonzero magnetic moment  $\boldsymbol{\mu}_p$  in external gradient magnetic field feels magnetic force  $\mathbf{F}_M = (\boldsymbol{\mu}_p \cdot \nabla) \mathbf{B}$ . If the particle is paramagnetic or superparamagnetic, increasing magnetic flux density  $B$  causes reorientation of particle domains into external flux density direction and from specific value ( $>500$  mT) its domains are fully reoriented and magnetically saturated. Therefore, the magnetic force on a magnetically saturated particle can be expressed as

$$\mathbf{F}_M = \mu_p \left| \left( \frac{\mathbf{B}}{B} \cdot \nabla \right) \mathbf{B} \right|, \tag{13}$$

where  $|\mu_p|$  is a magnetic moment magnitude of the saturated particle and the force is affected only with the gradient of magnetic field  $\mathbf{G}_M = ((\mathbf{B}/B) \cdot \nabla) \mathbf{B}$ .

For evaluation of a magnetic force contribution to the whole force exerted on particle it is necessary to know the magnetic field distribution  $\mathbf{B}$ . Analytically, it is possible only for simple sources of magnetic field, therefore, we have used for the description of used magnetic source a numerical method—the finite element method (FEM) and FEMM v4.2 (D. Meecker) software [28] as free toolbox for MATLAB (The MathWorks, Inc.).

*Magnetic Field Source – FEM model:* As a source of gradient magnetic field we have used octapolar magnet (kind of cylindrical Halbach array) compound of eight wedged Nd–Fe–B N37 magnets with magnetization direction revolving in  $135^\circ$  between adjacent blocks forming a cylinder with 28 mm as minimal inner and 90 mm as maximal outer diameter (same as in [29]). Octapolar magnet has been modeled in FEMM as 2D planar magnetostatic problem that corresponds to transversal section plane of infinite (or long enough) cylinder in 3D (i.e. flux density is defined in

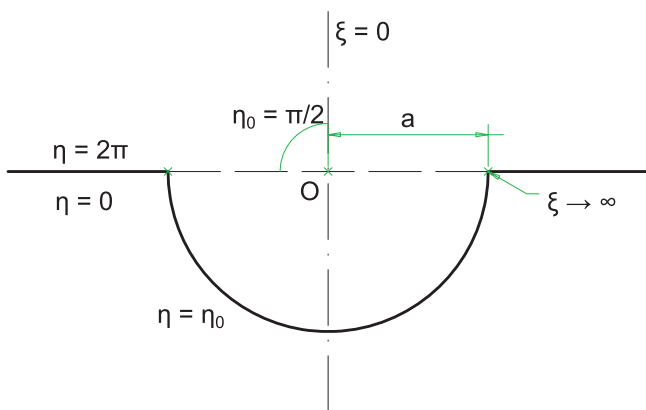


Fig. 1. The hemispherical-cap model of respiratory unit—alveolus.

$x_{FEMM}$ – $y_{FEMM}$  plane and its  $z_{FEMM}$  component equals to zero,  $B_{z_{FEMM}} = 0$  T). Magnetic field in cavity of cylinder has radial symmetry and its gradient in the center of alveolus location points in  $-y_{FEMM}$  axis direction. Center of alveolus was located in FEMM point  $[x_{c,FEMM}, y_{c,FEMM}] = [0.0, -7.5]$  mm (see Fig. 2). The maximal size of mesh elements in neighborhood of the center of alveolus with size of its maximal diameter (area of interest) has been chosen as  $0.5 \mu\text{m}$ , and in the corresponding  $\frac{1}{8}$  sector of cylindrical cavity was less than  $20 \mu\text{m}$ . In remaining domains it has been set to auto-choose mesh size and did not exceed 2 mm. Solution suitable for post-processing in MATLAB has been obtained with a mesh having totally over  $7 \times 10^5$  nodes.

Magnetic flux density value in queried points for magnetic force calculation is extracted from FEMM model directly using ActiveX support of MATLAB. Due to the fact, that output of FEMM is only a 2D model, and also that we have considered in simulations different cases of orientation of magnetic field gradient direction within the alveolus (default  $\mathbf{G}_M$  orientation is set to  $-y_{FEMM}$  axis direction, as has been mentioned previously), prior to general extraction of  $\mathbf{B}$  from FEMM it is necessary to transform the queried point location vector from the alveolus 3D Cartesian coordinate system,  $\mathbf{r} = [x, y, z]^T$ , to the FEMM 2D Cartesian coordinate system,  $\mathbf{r}_{FEMM} = [x_{FEMM}, y_{FEMM}]^T$ , in sense of general rotation, translation, and cutting of the third coordinate, i.e.

$$\begin{aligned} \mathbf{r}_{FEMM3D} &\equiv [x_{FEMM3D}, y_{FEMM3D}, z_{FEMM3D}]^T \\ &= \mathbf{R}(\alpha_r, \beta_r, \gamma_r) \cdot \mathbf{r} + [x_{c,FEMM}, y_{c,FEMM}, 0]^T, \end{aligned} \quad (14)$$

$$\mathbf{r}_{FEMM} \equiv [x_{FEMM}, y_{FEMM}]^T = [x_{FEMM3D}, y_{FEMM3D}]^T, \quad (15)$$

where  $\mathbf{R}(\alpha_r, \beta_r, \gamma_r)$  is general rotation matrix for vector rotation by angles  $\alpha_r$ ,  $\beta_r$ , and  $\gamma_r$  about  $x$ ,  $y$ , and  $z$  axes in three dimensions, respectively [30]. Extracted 2D magnetic flux density value from FEMM,

$$\mathbf{B}_{FEMM} \equiv [B_{x_{FEMM}}, B_{y_{FEMM}}]^T \quad (16)$$

in  $\mathbf{r}_{FEMM}$  point, has to be transformed *vice versa*, in sense of adding a third coordinate as zero value, and inverse rotation, i.e.  $\mathbf{B} = \mathbf{R}^{-1}(\alpha_r, \beta_r, \gamma_r) \cdot [B_{x_{FEMM}}, B_{y_{FEMM}}, 0]^T$ . These transformations are in principle transformation of one 3D Cartesian coordinate system (CCS) to another, by simple rotation and translation. Transformation matrix for location vector is therefore simple rotation matrix  $\mathbf{R}$  followed by translation; or for backward transformation of magnetic induction vector, transformation matrix is the inverse rotation matrix  $\mathbf{R}^{-1}$ . For better illustration see Fig. 3.

Partial differentiation of magnetic flux density in expression for gradient  $\mathbf{G}_M$  in each queried point during the simulation execution has been evaluated numerically by differentiation of magnetic flux density values in points in close proximity of queried point separated with distance  $\Delta r = 0.1 \mu\text{m}$ .

## 2.2. Magnetic particle specification

As particles for computer aided simulations we chose spheres of two different types. The first one was spheres of  $1 \mu\text{m}$  in diameter of magnetite with mass density  $5000 \text{ kg/m}^3$  and saturation magnetization  $478 \text{ kA/m}$ , and the second choice was droplets of  $3.5 \mu\text{m}$  in diameter of water aerosol with content of 2930 superparamagnetic iron-oxide nanoparticles (SPIONs) with the same concentration and properties as used in [31] for targeted delivery to the lungs of mice for both, experiment and simple simulation. Physical properties of fully magnetically saturated particles important for our computational modeling can be found in Table 1.

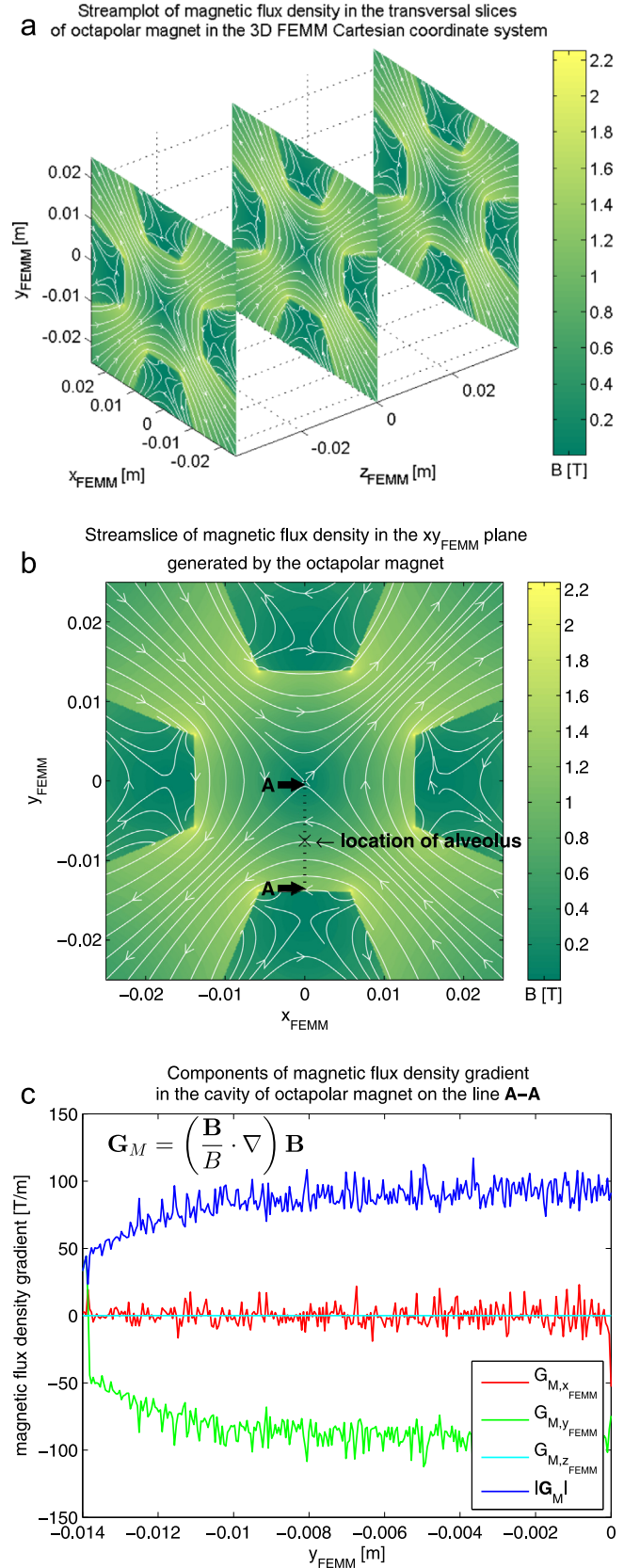


**Fig. 2.** FEM model of cylindrical Halbach array (octapolar magnet) as source of gradient magnetic field shown as (a) streamplots of magnetic flux density in several transversal slices of infinite octapolar magnet in the 3D FEMM Cartesian coordinate system (CCS), and (b) as streamslice in  $x_{FEMM}$ – $y_{FEMM}$  plane (the 2D FEMM CCS). Alveolus location is also shown (its center is in point  $[x_{c,FEMM}, y_{c,FEMM}] = [0.0, -7.5]$  mm). (c) The components of magnetic flux density gradient ( $\mathbf{G}_M$ ) on the line A-A are also shown. Gradient in the center of alveolus location points in  $-y_{FEMM}$  axis direction, reaches value  $\approx 100$  T/m and can be considered as homogeneous in the volume of alveolus.

### 2.3. ODEs governing motion

After consideration of all assumptions mentioned, the system of ordinary differential equations (ODEs) governing motion of single magnetic particle (single particle problem) under the influence of gradient magnetic and gravitational field, and Stokesian viscous flow fields of rhythmically expanding and contracting hemispherical alveolus can be expressed as single ODE in vector notation as

$$\frac{d^2 \mathbf{r}_p}{dt^2} = \left[ \mu_p \left( \frac{\mathbf{B}(\mathbf{r}_p)}{B(\mathbf{r}_p)} \cdot \nabla \right) \mathbf{B}(\mathbf{r}_p) + \mathbf{F}_D(\mathbf{r}_p, t) + m_p \mathbf{g} \right] / m_p, \quad (17)$$

where  $\mathbf{F}_D(\mathbf{r}_p, t)$  will be substituted with (12).

### 3. Results and discussion

As primary software for particle trajectory calculation we have used MATLAB R2013a (The Mathworks, Inc.), particularly `ode15s` solver as a tool for solving stiff systems of ODEs based on the numerical differentiation formulas [32]. Trajectories of particles have been evaluated for each type and each particle as a single particle problem described with ODEs (17) with equally spaced initial position in the longitudinal section plane of the hemispherical alveolus attached to the ductus (Fig. 4(a)). Magnetic field distribution extracted from FEMM with direction of gradient in  $-y_{\text{FEMM}}$  axis has been in different cases of simulation oriented into or out-off alveolar cavity, or in proximal or distal direction of acinus (by specification of angles  $(\alpha_r, \beta_r, \gamma_r)$  in general rotation matrix  $\mathbf{R}$ ), as well as relatively to different directions of gravitational acceleration vector  $\mathbf{g}$ . Simulations have been done for alveolus with the following geometrical and physiological properties:  $R_0 = 150 \mu\text{m}$  and  $\beta = 0.1$  as average alveolus diameter and its relative amplitude, respectively,  $\gamma = 300$  what corresponds to flow in  $\approx 21$ st airway generation in pulmonary acinus. We have also considered zero phase difference between shear and expansion

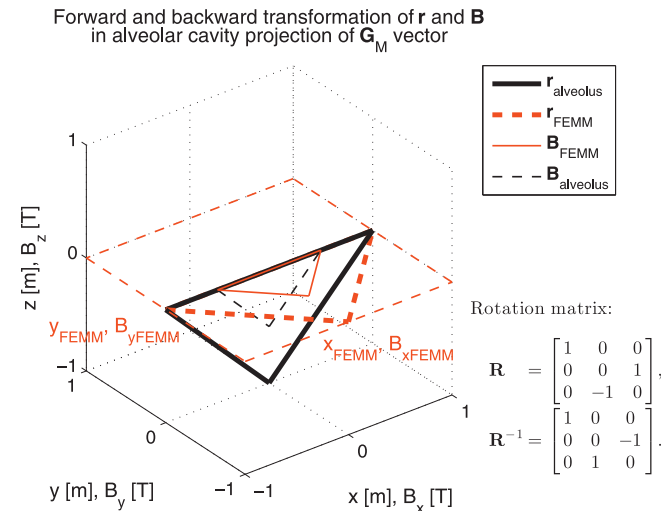


**Fig. 3.** Forward transformation of the location vector  $\mathbf{r} = [0.0, 0.0, -1.0]$  m (but without translation) from the alveolus 3D Cartesian coordinate system (CCS) (black) to the FEMM 2D CCS (red), and backward transformation of the magnetic induction vector  $\mathbf{B} = [0.0, -0.5]$  T from the FEMM 2D CCS (with added third zero value coordinate) to the alveolus 3D CCS. The shown transformations are transformations in alveolar cavity projection of  $\mathbf{G}_M$  vector (i.e.,  $\mathbf{G}_M$  vector points in  $-z$  axis direction in alveolus 3D CCS—same as in Fig. 4(f) or Fig. 7). Vectors are shown as isosceles triangles in transformed planes. A magnitude of the vectors is proportional to the height of the triangles. (For interpretation of the references to color in this figure caption, the reader is referred to the web version of this paper.)

**Table 1**

Parameters of particles used in simulations.

Quantity	Magnetite sphere	Droplet wSPIONs <sup>a</sup>
Diameter, $D_p$ (m)	$1.0 \times 10^{-6}$	$3.5 \times 10^{-6}$
Mass, $m_p$ (kg)	$2.6 \times 10^{-15}$	$22.9 \times 10^{-15}$
M. moment <sup>b</sup> , $ \mu_p $ (A m <sup>2</sup> )	$250 \times 10^{-15}$	$26.4 \times 10^{-15}$

<sup>a</sup> Water aerosol droplet with content of 2930 SPIONs. Single SPION is 80 nm in diameter with core 50 nm in diameter. Core comprises 5 nm single domain magnetite nanoparticles with packaging density of 30% and adsorbed 15 nm PEI 25 kDa layer dispersed in water. For details see Supplementary information of [31].

<sup>b</sup> Magnetic moment of fully magnetically saturated particle.

(i.e. ductal and alveolar) flow, i.e.  $\delta = 0^\circ$ , and breathing frequency 12 breaths-per-minute.

Simulations for several model configurations have been performed. Some of them for water aerosol droplets (with content of SPIONs) used as particles are figured as their trajectories in Fig. 4. In the gravity-free and magnetic-free configuration, Fig. 4(b), particles painted rhythmically periodic trajectories and were captured only if their initial position was too close to the proximal wall of alveolus cavity due to contraction of hemispherical alveolus during expiration which the simulation started from. In the other cases we have compared effect of applied gravity and gradient magnetic field both, independently and collectively, with influence of aerodynamic viscous drag force on particle due to rhythmical expansion of alveolus and alternating shear flow, as you can see in Fig. 4(c–f). Magnetic force exerted on a particle has a major effect in comparison with both, gravitational force and aerodynamic viscous drag in the used source of gradient magnetic field and chosen airway generation represented with  $\gamma = 300$  value for ductal flow. Ascendance of magnetic force over gravity is obvious when we realize physical properties of used particles (for both, magnetite spheres and droplets with SPIONs; see Table 1) and magnitude of gradient of magnetic field generated in cavity of cylindrical Halbach array reaching the value almost  $G_M \approx 100$  T/m, what yields in the case of the aerosol droplets with SPIONs used as particle magnetic force more than 10 times (in the case of used magnetite spheres it is even more – about 1000 times) stronger force than gravity. Magnitude of changing aerodynamic viscous drag force on each particle is not so obvious during rhythmical breathing (for better illustration see for instance Fig. 6). But, for chosen  $\gamma$  value, magnetic force exerted on used particles can easily overcome viscous drag (even if gravity has the same direction as instantaneous aerodynamic viscous drag flow or opposite direction to magnetic gradient) and cause movement of particles in the direction of magnetic gradient (Fig. 4(d, f)), what can lead to deposition of particles in the alveolus cavity during the first breathing period (see Fig. 4(f)). Gravity field alone can also overcome aerodynamic viscous drag force and cause deposition of particles, see Fig. 4(c).

The same situation as in Fig. 4(c, d) but for perpendicular direction of gradient of magnetic field relative to vertical gravitational field is shown in Fig. 5. The gradient of magnetic field has proximal, lateral and distal direction in Fig. 5(a–c), respectively. Ascendance of magnetic force over gravitational and aerodynamic forces in the studied configurations is obvious, too.

The same calculation for proximal airway generation with immense ascendance of ductal flow ( $\gamma = 1000$ ) shows that deposition induced with gradient magnetic field can overcome both, sedimentation and aerodynamic viscous drag flow (see Fig. 7).

We have further studied how critical are parameter values to the obtained results. Simple insight can be obtained from the results of simulations shown in Fig. 8. When it was considered the beginning of expiration as the initial time of movement from

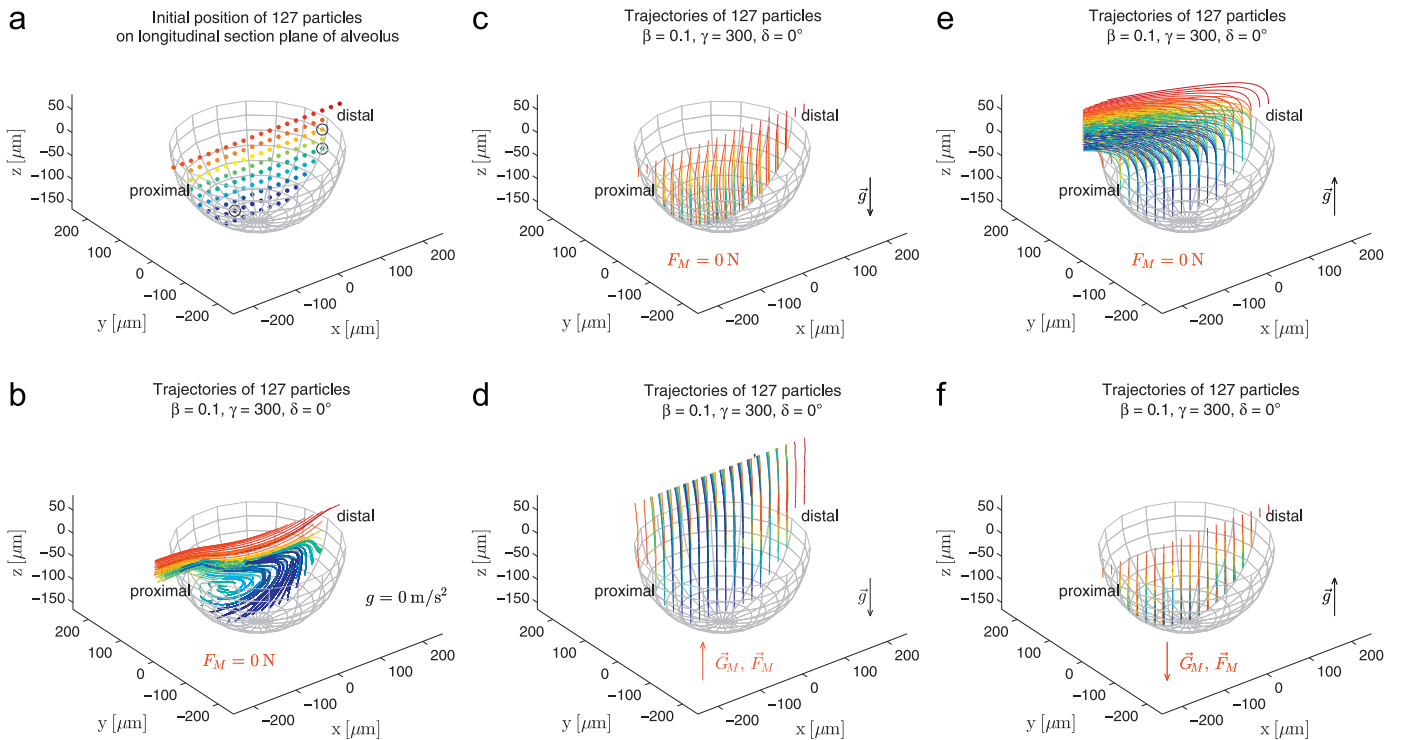


**Fig. 4.** Simulation of motion of particles – water aerosol droplets with content of SPIONs – with exerting influence of aerodynamic viscous drag force due to rhythmical expansion and alternating shear flow in alveolus, and gravity and magnetic force during 20 breathing periods starting with expiration, shown as trajectories of particles: (a) initial position equally spaced in longitudinal section plane of alveolus (300  $\mu\text{m}$  in diameter); (b) in gravity-free and magnetic-free conditions; (c, e) under the influence of gravitational field and viscous drag force; and (d, f) viscous drag force affected by gravitational and gradient magnetic field with mutual inverse vector orientation (particles and their trajectories are distinguished with different colors). (For interpretation of the references to color in this figure caption, the reader is referred to the web version of this paper.)

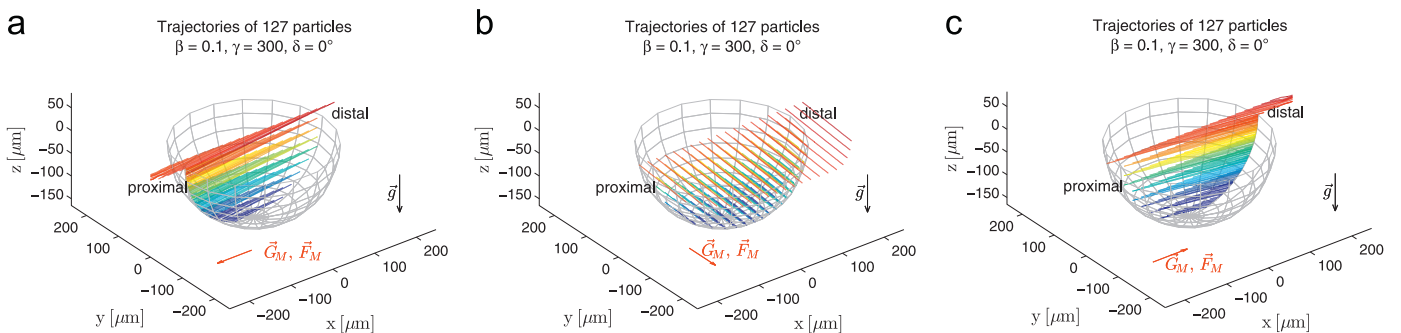


**Fig. 5.** Trajectories of water aerosol droplets with content of SPIONs with exerting influence of aerodynamic viscous drag force due to rhythmical expansion and alternating shear flow in alveolus, and gravity and magnetic force. Simulations started with expiration. Gravitational field has vertical direction and is perpendicular relative to the direction of gradient of magnetic field in the cavity of octapolar magnet. Three different configurations in subfigures are shown: gradient of magnetic field has (a) proximal, (b) lateral, and (c) distal direction downstream of acinar ductus and alveolus. Initial position of particles was the same as in Fig. 4—equally spaced in longitudinal section plane of alveolus (300  $\mu\text{m}$  in diameter). Particle trajectory calculations were stopped due to reaching of the alveolus wall or boundary of calculation domain (particles and their trajectories are distinguished with different colors). (For interpretation of the references to color in this figure caption, the reader is referred to the web version of this paper.)

initial position in alveolar and paravascular space (Fig. 8(a), where  $\varphi_0$  equals zero as an initial phase in  $R_{l=0} = R_0(1 + \beta \cos \varphi_0)$ ), the particles were affected minimally by choice of the value of physiological parameter  $\gamma$  (specifically: 300 and 1000, for distal and proximal locations of alveolus downstream the acinar tree, respectively) or parameter  $\delta$  (specifically:  $10^\circ$  and  $0^\circ$ , for physiological value and the value for simplification of the model, respectively). Magnetic force prevailed significantly over other interactions, and it led to very fast magnetically induced deposition of particles during the first breathing period without significant change of trajectories due to aerodynamic and gravitational force. On the other hand, when it was considered the middle of expiration (i.e. when the velocity of flow in ductus and alveolus

reaches its maximal values) as the initial time of movement in simulations (Fig. 8(b), the initial phase is  $\varphi_0 = \pi/4$ ), movement of particles was more sensitive to choice of parameter values, as can be seen on different trajectories for different cases, especially for large values of  $\gamma$  in paravascular and alveolar space near opening of alveolus. However, magnetic force succeeded to overcome both, aerodynamic and gravitational, forces exerting on particles and induced their deposition. The change of the value of parameter  $\delta$  had in simulations minimal effect on deposition of particles induced by magnetic force.

Expiration has been used as the initial time of movement in the majority of presented results of simulations. It represents situation, when the particles are in the beginning of motion already

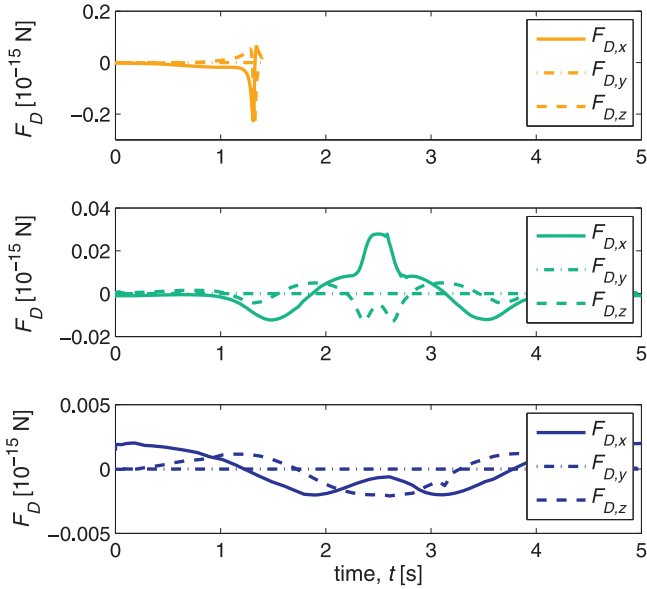


**Fig. 6.** Drag force exerted on particle of  $3.5\ \mu\text{m}$  in diameter (aerosol droplet with SPIONs) during first breathing period (starting with expiration) in gravity-free and magnetic-free conditions for alveolus with  $\beta = 0.1$ ,  $\gamma = 300$ , and  $\delta = 0^\circ$  (corresponds to Fig. 4(b)) for particle in three different initial positions highlighted with black  $\circ$  in Fig. 4(a) (particles and their time evolution of exerting drag force are distinguished with different colors). In the first case was the calculation of particle trajectory stopped due to reaching the boundary of calculation domain. (For interpretation of the references to color in this figure caption, the reader is referred to the web version of this paper.)

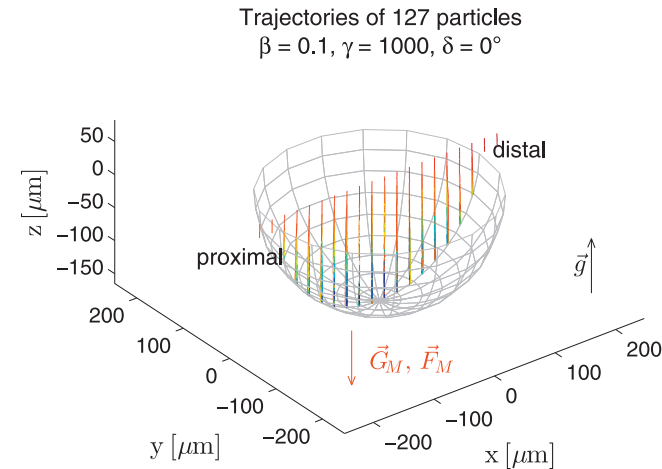


**Fig. 7.** Simulation of motion of particles – water aerosol droplets with content of SPIONs – with exerting influence of aerodynamic viscous drag force due to rhythmical expansion and alternating shear flow in alveolus, and gravity and magnetic force during 20 breathing periods starting with expiration, shown as trajectories of particles. Calculated for alveolus in proximal airway generation ( $\beta = 0.1$ ,  $\gamma = 1000$ , and  $\delta = 0^\circ$ ; initial position same as in Fig. 4(a)). Particles and their trajectories are distinguished with different colors. (For interpretation of the references to color in this figure caption, the reader is referred to the web version of this paper.)

presented in alveolus or paravascular space and quiescent, and had already get to this place from ductus in previous breathing periods. Used physical model is best suited for alveolar and paravascular ductal space.

As it has been studied earlier, particles in gravity-free conditions under the influence of aerodynamic drag forces in alveolus during breathing, will deposit due to geometrical interception mechanism [19], what is caused primarily by non-zero value of phase difference  $\delta$  between ductal and alveolar flows occurring

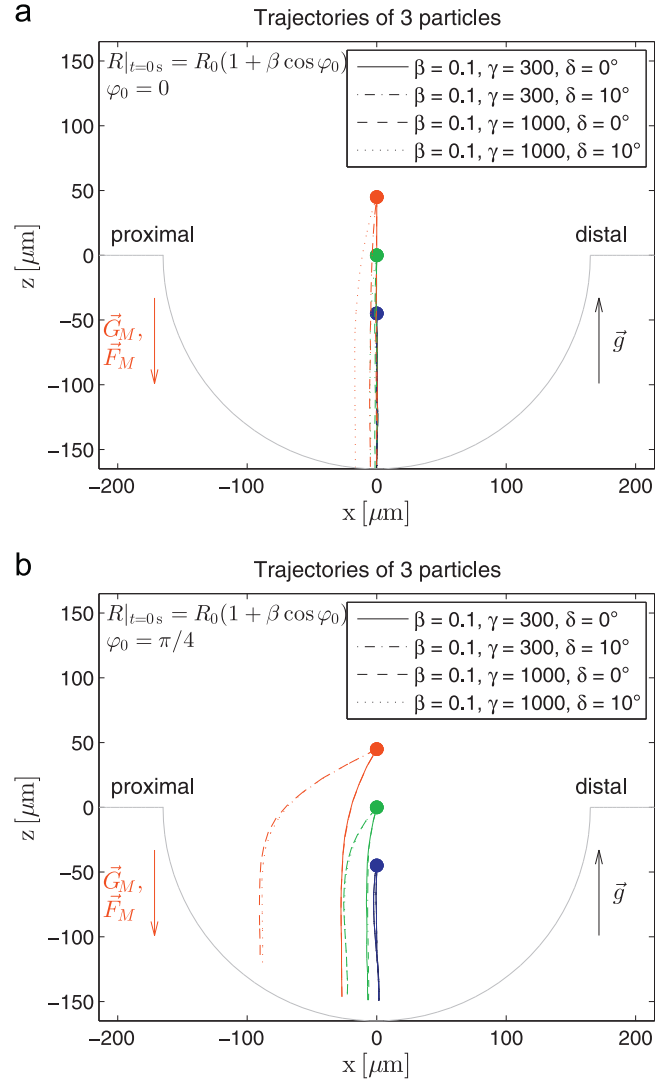


**Fig. 8.** Trajectories of particle (water aerosol droplet with content of SPIONs) from three different initial positions on  $z$ -axis of Cartesian coordinate system (red, green and blue) exerting influence of aerodynamic viscous drag force due to rhythmical expansion and alternating shear flow in alveolus, and gravity and magnetic force. Simulations started (a) from the beginning of expiration ( $\varphi_0 = 0$ ; similar to situations in Figs. 4–7), or (b) from the middle of expiration ( $\varphi_0 = \pi/4$ ), where  $\varphi_0$  is an initial phase; and were done for four different combinations of values of physiological parameters  $\gamma$  and  $\delta$ . (For interpretation of the references to color in this figure caption, the reader is referred to the web version of this paper.)

during breathing. A reason why we assume zero value of  $\delta$  in our simulations was the fact that we wanted to compare magnetic induced deposition of particles with the magnitude of forces of aerodynamic viscous drag flows during breathing without premature capturing of particles with acinus wall due to geometrical interception mechanism. Naturally, this will have a synergistic effect on deposition in reality, but will not increase the magnitude of aerodynamic viscous drag forces induced with flows.

Finally, it is necessary discuss, how critical is the magnetization of particles to the obtained results. Influence of magnetization degree to the magnetic force acting on particle is linear. Therefore, magnitude of magnetic force (at constant magnitude of gradient  $G_M = |\mathbf{G}_M|$ ) can be estimated directly from magnetic properties of used particles— Table 1. As well, it can be estimated that magnetic force acting on magnetite spheres is approximately 10 times larger than for aerosol droplets with content of SPIONs, and therefore, deposition of magnetite spheres induced with gradient magnetic field will be more rapid in comparison with droplets with SPIONs,

i.e., it is not necessary to show results for this case explicitly. Also, used source of magnetic field (cylindrical Halbach array) generates in its air cavity field, whose magnitude of magnetic flux density in the most of this space (except the central paraxial region) is  $>0.5$  T, which corresponds to magnetic intensity  $>400$  kA/m. At this intensity, magnetic particles can be considered as fully magnetically saturated, and used physical model as suitable. For weaker magnetic fields, it will be convenient to incorporate to calculation of particle magnetic moment also degree of magnetization dependent on intensity of external magnetic field by using particle magnetization curve. However, after placing mice to the cavity of studied cylindrical Halbach array, there will be localized only mediastinum in the central paraxial region with weaker magnetic field, and on the other hand, there will be own lung tissue in the most of remaining space of cavity. Therefore improvement of our model for weaker magnetic field is not necessary.

#### 4. Conclusion

As has been clearly demonstrated in this study, magnetically induced deposition of particles can overcome both, aerodynamic viscous drag forces in alveolus and their gravitational sedimentation, not only in the case of particles with large magnetic moment (magnetite spheres), but also in the case of water aerosol droplets containing SPIONS, whose magnetic moment is reduced in comparison with magnetite spheres. Moreover, this effect occurs not only in distal airway generations with reduced ductal flows, but also in proximal ones.

#### Acknowledgment

The authors would like to thank Grant Agency of the Slovak Academy of Sciences (VEGA 2/0013/14 and VEGA 1/0871/14) for financial support; and MATLAB Cluster CVTI Bratislava, Slovakia, where the computations were done.

#### References

- [1] M. Babincova, K. Kontriso, S. Durdik, C. Bergemann, P. Sourivong, Radiation enhanced efficiency of combined electromagnetic hyperthermia and chemotherapy of lung carcinoma using cisplatin functionalized magnetic nanoparticles, *Pharmazie* 69 (2) (2014) 128–131. <http://dx.doi.org/10.1691/ph.2014.3708>.
- [2] J. Rosenecker, The long and winding road to clinical success in gene therapy, *Curr. Opin. Mol. Ther.* 12 (5) (2010) 507–508.
- [3] M. Babincova, P. Babinec, Aerosolized VEGF in combination with intravenous magnetically targeted delivery of DNA-nanoparticle complex may increase efficiency of cystic fibrosis gene therapy, *Med. Hypotheses* 67 (4) (2006) 1002. <http://dx.doi.org/10.1016/j.mehy.2006.05.001>.
- [4] P. Babinec, M. Babincova, Genetically engineered bacteria may be useful for delivery of mucolytics into cystic fibrosis lungs, *Med. Hypotheses* 67 (2) (2006) 426–427. <http://dx.doi.org/10.1016/j.mehy.2006.03.013>.
- [5] S. Durdik, A. Krafčík, M. Babincova, P. Babinec, Conceptual design of integrated microfluidic system for magnetic cell separation, electroporation, and transfection, *Phys. Med.* 29 (5) (2013) 562–567. <http://dx.doi.org/10.1016/j.ejmp.2012.11.003>.
- [6] S. Durdik, H. Vrbovska, A. Olas, M. Babincova, Influence of naturally occurring antioxidants on magnetic nanoparticles: risks, benefits, and possible therapeutic applications, *Gen. Physiol. Biophys.* 32 (2) (2013) 173–177. <http://dx.doi.org/10.4149/gpb-2013039>.
- [7] S. Durdik, M. Babincova, C. Bergemann, P. Babinec, Nanosecond laser pulse induced stress waves enhanced: magnetofection of human carcinoma cells in vitro, *Laser Phys. Lett.* 9 (9) (2012) 678–681. <http://dx.doi.org/10.7452/lapl.201210064>.
- [8] M. Babincova, P. Babinec, Magnetic drug delivery and targeting: principles and applications, *Biomed. Papers* 153 (4) (2009) 243–250.
- [9] A. Krafčík, M. Babincova, P. Babinec, Theoretical analysis of magnetic particle trajectory in high-current pulsed quadrupole: implications for magnetic cell separation, drug targeting, and gene therapy, *Optoelectron. Adv. Mater. Rapid Commun.* 3 (3) (2009) 226–230.
- [10] M. Babincova, V. Altanerova, C. Altaner, C. Bergemann, P. Babinec, In vitro analysis of cisplatin functionalized magnetic nanoparticles in combined cancer chemotherapy and electromagnetic hyperthermia, *IEEE Trans. Nanobiosci.* 7 (1) (2008) 15–19. <http://dx.doi.org/10.1109/TNB.2008.2000145>.
- [11] M. Babincova, P. Babinec, C. Bergemann, High-gradient magnetic capture of ferrofluids: implications for drug targeting and tumor embolization, *Z. Naturforschung—Sect. C J. Biosci.* 56 (9–10) (2001) 909–911.
- [12] U. Hafeli, K. Saatchi, P. Elischer, R. Misri, M. Bokharaei, N. Renée Labiris, B. Stoeber, Lung perfusion imaging with monosized biodegradable microspheres, *Biomacromolecules* 11 (3) (2010) 561–567. <http://dx.doi.org/10.1021/bm9010722>.
- [13] U. Hafeli, J. Riffle, L. Harris-Shekhawat, A. Carmichael-Baranauskas, F. Mark, J. Dailey, D. Bardenstein, Cell uptake and in vitro toxicity of magnetic nanoparticles suitable for drug delivery, *Mol. Pharm.* 6 (5) (2009) 1417–1428. <http://dx.doi.org/10.1021/mp900083m>.
- [14] G. Hasenpusch, J. Geiger, K. Wagner, O. Mykhaylyk, F. Wiekhorst, L. Trahms, A. Heidsieck, B. Gleich, C. Bergemann, M. Aneja, C. Rudolph, Magnetized aerosols comprising superparamagnetic iron oxide nanoparticles improve targeted drug and gene delivery to the lung, *Pharm. Res.* 29 (5) (2012) 1308–1318. <http://dx.doi.org/10.1007/s11095-012-0682-z>.
- [15] G. Hatch, R. Stelter, Magnetic design considerations for devices and particles used for biological high-gradient magnetic separation (HGMS) systems, *J. Magn. Magn. Mater.* 225 (1–2) (2001) 262–276. [http://dx.doi.org/10.1016/S0304-8853\(00\)01250-6](http://dx.doi.org/10.1016/S0304-8853(00)01250-6).
- [16] E. Danieli, J. Perlo, B. Blumich, F. Casanova, Highly stable and finely tuned magnetic fields generated by permanent magnet assemblies, *Phys. Rev. Lett.* 110 (18) (2013) 180801. <http://dx.doi.org/10.1103/PhysRevLett.110.180801>.
- [17] S. Haber, J.P. Butler, H. Brenner, I. Emanuel, A. Tsuda, Shear flow over a self-similar expanding pulmonary alveolus during rhythmical breathing, *J. Fluid Mech.* 405 (2000) 243–268.
- [18] S. Haber, D. Yitzhak, A. Tsuda, Gravitational deposition in a rhythmically expanding and contracting alveolus, *J. Appl. Physiol.* 95 (2) (2003) 657–671.
- [19] S. Haber, D. Yitzhak, A. Tsuda, Trajectories and deposition sites of spherical particles moving inside rhythmically expanding alveoli under gravity-free conditions, *J. Aerosol Med. Pulm. Drug Deliv.* 23 (6) (2010) 405–413. <http://dx.doi.org/10.1089/jamp.2009.0774>.
- [20] J. Heyder, J. Gebhart, G. Scheuch, Interaction of diffusional and gravitational particle transport in aerosols, *Aerosol Sci. Technol.* 4 (3) (1985) 315–326.
- [21] C. Pozrikidis, Shear flow over a plane wall with an axisymmetric cavity or a circular orifice of finite thickness, *Phys. Fluids* 6 (1) (1994) 68–79.
- [22] A. Tsuda, Y. Otani, J.P. Butler, Acinar flow irreversibility caused by perturbations in reversible alveolar wall motion, *J. Appl. Physiol.* 86 (3) (1999) 977–984.
- [23] B. Haefeli-Bleuer, E.R. Weibel, Morphometry of the human pulmonary acinus, *Anatom. Rec.* 220 (4) (1988) 401–414.
- [24] J. Happel, H. Brenner, *Low Reynolds Number Hydrodynamics—with Special Applications to Particulate Media*, Kluwer, Boston, MA, USA, 1983.
- [25] M.I. Zhurina, L.N. Karmazina, *Tables and Formulae for the Spherical Functions  $P_{-1/2+iq}^m(z)$* , Pergamon, London, UK, 1966.
- [26] C. Pozrikidis, *A Practical Guide to Boundary-Element Methods with the Software Library BEMLIB*, Chapman & Hall/CRC Press, London, UK, 2000.
- [27] C. Pozrikidis, FDLIB v.13.10—Fluid Dynamics Software Library, available [online] (April 2014). (<http://dehesa.freeshell.org/FDLIB/fdlib.shtml>).
- [28] D. Meeker, FEMM v.4.2—Finite Element Method Magnetics, available [online] (April 2014). (<http://www.femm.info/wiki/HomePage>).
- [29] P. Babinec, A. Krafčík, M. Babincova, J. Rosenecker, Dynamics of magnetic particles in cylindrical Halbach array: implications for magnetic cell separation and drug targeting, *Med. Biol. Eng. Comput.* 48 (8) (2010) 745–753. <http://dx.doi.org/10.1007/s11517-010-0636-8>.
- [30] E.W. Weisstein, Rotation matrix, From MathWorld—A Wolfram Web Resource, available [online] (April 2014). (<http://mathworld.wolfram.com/RotationMatrix.html>).
- [31] P. Dames, B. Gleich, A. Flemmer, K. Hajek, N. Seidl, F. Wiekhorst, D. Eberbeck, I. Bittmann, C. Bergemann, T. Weyh, L. Trahms, J. Rosenecker, C. Rudolph, Targeted delivery of magnetic aerosol droplets to the lung, *Nat. Nanotechnol.* 2 (8) (2007) 495–499. <http://dx.doi.org/10.1038/nnano.2007.217>.
- [32] L.F. Shampine, M.W. Reichelt, The MATLAB ode suite, *SIAM J. Sci. Comput.* 18 (1) (1997) 1–22.